Article

Magnetite Fe3O4 (111) Surfaces: Impact of Defects on Structure, Stability, and Electronic Properties

Junghyun Noh, Osman I Osman, Saadullah G. Aziz, Paul Winget, and Jean-Luc Bredas

Just Accepted

Magnetite Fe$_3$O$_4$ (111) Surfaces: Impact of Defects on Structure, Stability, and Electronic Properties

Junghyun Noh,[†,‡,‖] Osman I. Osman,[§] Saadullah G. Aziz,[§] Paul Winget,[†] and Jean-Luc Brédas[‖,†,*]

[†] School of Chemistry and Biochemistry and Center for Organic Photonics and Electronics, Georgia Institute of Technology, Atlanta, Georgia 30332-0400

[‡] School of Materials Science and Engineering, Georgia Institute of Technology, Atlanta, Georgia 30332-0245

[§] Department of Chemistry, Faculty of Science, King Abdulaziz University, P.O. Box 80203, Jeddah 21589, Kingdom of Saudi Arabia

[‖] Solar and Photovoltaics Engineering Research Center, Division of Physical Science and Engineering, King Abdullah University of Science and Technology – KAUST, Thuwal 23955-6900, Kingdom of Saudi Arabia

1 **Abstract**

2 We present a comprehensive investigation, via first-principles density functional theory

3 (DFT) calculations, of various surface terminations of magnetite, Fe_3O_4 (111), a major

4 iron oxide which has also a number of applications in electronics and spintronics. We

5 compare the thermodynamic stability and electronic structure among the different

6 surfaces terminations. Interestingly, we find that surfaces modified with point defects

7 and adatoms are close in surface energy and in the oxygen-rich and oxygen-poor

8 regimes can be more stable than bulk-like terminations. These surfaces show different

9 surface chemistry and electronic structures as well as distinctive spin polarization

10 features near the Fermi level with regard to those previously considered in the literature.

11 Our studies provide an atomic level insight for magnetite surfaces, which is a necessary

12 step to understanding their interfaces with organic layers in OLED and spintronic

13 devices.

14

15 **Table of Contents**

16

17

18

19
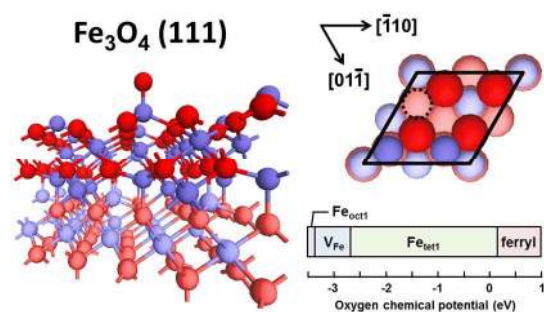
1   **I. Introduction**

2   Iron oxides, particularly magnetite (Fe_3O_4), have attracted interest in numerous fields

3   including environmental remediation,[1] biophysics,[2] electrochemistry,[3] sensors,[4] and

4   catalysis.[5] Fe_3O_4 has also been exploited in organic light-emitting diodes (OLEDs). For

5   example, magnetite electrodes can prevent the short-circuit problems seen in

6   conventional top metallic electrodes as the diffusivity of the oxide species is much lower

7   than its metallic counterparts, and have been successfully deposited on top of tris (8-

8   hydroxyquinoline) aluminum(III) (Alq_3).[6] Moreover, the use of a thin Fe_3O_4 layer on

9   indium-tin-oxide (ITO)[7] and Ag[8] anodes has been shown to enhance hole injection and

10   thus reduce turn-on voltage and enhance luminance and current density in devices.

11   A major potential application of this iron oxide is as an electrode in spintronic devices

12   where spin functionality is built into hybrid organic devices.[9] While there have been

13   many materials considered so far as a source of spin injection, including ferromagnetic

14   (FM) metals,[10] dilute magnetic semiconductors,[11] and Heusler alloys,[12] half-metallic

15   ferro- (or ferri-) magnetic oxides[13-14] can produce a very high magnetoresistive (MR)

16   response. In particular, advantages for using magnetite as an electrode in such devices

17   include its high degree of spin polarization at the Fermi level, high Curie temperature

18   (850 K), and the ability to grow high-quality films at room temperature,[15] although device

19   performance remains underwhelming.[16] As the performance of these devices is dictated

20   by the electronic structure immediately at the interface, a fundamental knowledge of the

21   surface chemistry is required. For a spin field-effect transistor, the spin– injection and

22   detection efficiencies are required to be 99.9995% to achieve the 10^5 on-off ratio

23   needed in mainstream applications.[17] In the case of surface electronic states on a clean

3

1   Fe_3O_4 (001) surface, from 65%[18] to less than 5% of electron-spin polarization at the

2   Fermi-level has been observed.[19-20] Thus, even small contributions to the electrode's

3   electronic structure from defects are of essential importance. However, the study of

4   hybrid interfaces between magnetite and organic layers remains in its infancy. The

5   electronic structure of magnetite varies qualitatively depending on the surface

6   orientation and termination.[21-22] Additional complexity is introduced as the control of the

7   stoichiometry is highly dependent on the preparation conditions.[23]

8   Bulk magnetite is a ferrimagnet with a cubic inverse spinel structure, with a chemical

9   formula often written as $[Fe^{3+}]_A[Fe^{3+},Fe^{2+}]_BO_4$.   This formula indicates that the

10 tetrahedral sites denoted as A are occupied by ferric ions while octahedral sites denoted

11 as B contain an equal number of ferric and ferrous ions. In magnetite, the tetrahedral

12 and octahedral sites form two magnetic sublattices with the spin moments on the A

13 sublattice antiparallel to those on the B sublattice. The proposed electronic structure of

14 the octahedral Fe^{2+} cations corresponds to a situation where an extra electron resides

15 in the lowest unoccupied t_{2g} orbital located at the Fermi level. The high electrical

16 conductivity of 2×10^2 S/cm[24] in the thermodynamic standard state can be understood

17 as resulting from rapid electron hopping processes between Fe^{2+} and Fe^{3+} ions.

18 However, upon cooling below ~121 K (T_V), magnetite undergoes a Verwey phase

19 transition,[25] with the electronic conductivity decreasing by two orders of magnitude and

20 an associated opening of the optical gap.[26] This transition is also accompanied by a

21 structural distortion from the room temperature cubic system.[27-29]

22 Several surface faces of magnetite have been prepared by varying the preparation

23 conditions, including (100), (111), (110), (311), (331), and (511).[30-34]   Some of these

4

1   facets have been thoroughly investigated previously, for example, the (100) surface, [30,]

2   [35-36] which has recently been shown to have $(\sqrt{2} \times \sqrt{2})R45°$-reconstructed B termination

3   with assistance of iron vacancies and interstitials in the subsurface.[37] In the present

4   study, we have chosen to focus on the Fe_3O_4 (111) plane since: (i) it is the predominant

5   natural cleavage plane; and (ii) it is the plane compatible with the hematite (α-Fe_2O_3)

6   (0001) surface that is regarded thermodynamically as the most stable at ambient

7   conditions. However, α-Fe_2O_3 does not grow epitaxially on Fe_3O_4(111), the cause of

8   which remains a topic of study.[38] Additionally, in comparison to the other natural growth

9   faces of Fe_3O_4, Yu *et al.*[39] found a higher stability of the (111) surface within a DFT+U

10   scheme.

11   Here, our goal is to present a comprehensive DFT investigation, using generalized

12   gradient approximation (GGA)+U approach, to describe the electronic and magnetic

13   features of room-temperature magnetite surfaces. This understanding represents a

14   necessary step prior to extending our calculations to interfaces with organic layers seen

15   in OLED and spintronic devices. The calculations presented here provide a thorough

16   analysis of the various magnetite (111) surface terminations in terms of thermodynamic

17   stabilities, surface electronic structures, and surface chemical properties. Our results

18   underline the possible stabilization of the Fe_3O_4 (111) surface via introduction of point

19   defects and adatoms. Importantly, our work demonstrates that four modified surfaces

20   not considered in earlier theoretical studies show comparable surface stabilities to bulk

21   truncated terminations but with significantly different surface chemistry and

22   electronic/magnetic features. They thus appear to be of critical importance when

23   developing atomistic models for magnetite interfaces.

1

II. Methodology

a) Terminations examined

The magnetite crystal contains layers of either only iron cations or oxygen anions along the [111] direction with the stacking sequence: O_1-Fe_{oct1}-O_2-Fe_{tet2}-Fe_{oct2}-Fe_{tet1}, as displayed in Figure 1; this leads to six unique atomic planes, where we follow the conventional notations to refer to each of the six bulk terminations.[23] The four iron terminations can present two different Fe sublayers; one is a dense monolayer (3/4ML) with all octahedrally coordinated Fe atoms (Fe_{oct1}) on the same plane, while the other sublayer contains three distinct low-density monolayers (1/4ML) involving both octahedrally and tetrahedrally coordinated Fe atoms (Fe_{tet2}-Fe_{oct2}-Fe_{tet1}). Those two iron sublayers are alternating between nearly close-packed oxygen stacking layers (1ML) that present a slight buckling. As the number and charge of the iron and oxygen ions on the surface differ, Fe_3O_4 (111) can be classified as a type-3 surface in the Tasker classification scheme,[40] with diverging electrostatic surface energy due to the presence of a non-zero dipole moment on all the repeat units throughout the material. In order to decrease the internal polarity perpendicular to the surface, major ionic relaxation and electron redistribution as well as surface reconstruction are expected;[22] in spite of multiple studies involving various surface science techniques and computational approaches, the atomistic details of the Fe_3O_4 (111) surface are still a matter of debate as the exposed surface depends strongly on the preparation conditions and chemical environment. As the spin-polarization, resistivity, and Verwey transition are dependent

6

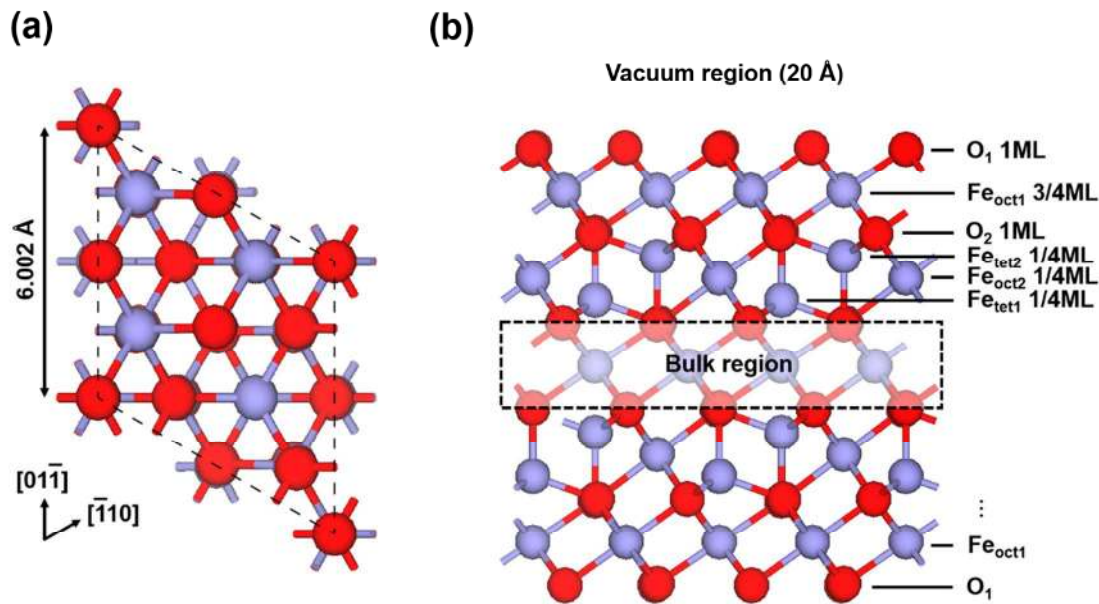1　on the exact stoichiometry of thin films, development of an atomic-level description is

2　vital.

Figure 1 (a) Top view and (b) side view of the symmetric Fe_3O_4 (111) slab model. The stacking sequence, labeled O_1-Fe_{oct1}-O_2-Fe_{tet2}-Fe_{oct2}-Fe_{tet1}, is shown in panel (b). Fe atoms are colored blue, and oxygen ions are colored red.

8　At this stage, it is useful to recall a number of previous observations regarding

9　magnetite surfaces. Scanning tunneling microscopy (STM) study of Fe_3O_4 (111)

10　annealed at 1173 K in 2×10^{-7} mbar O_2 reported a coexisting surface termination

11　composed of a hexagonal array of 6.1 Å and a honeycomb pattern separated by 3.6

12　Å.[41] The authors assigned the second pattern to termination to 2/4 ML of Fe atoms

13　which is predicted to be more stable than the former, 3/4 ML capped by an O atom. In a

14　later paper, the same authors reexamined the surface structure of single crystal UHV-

15　prepared Fe_3O_4 (111) and concluded that the surface mainly consists of Fe_{tet1}, Fe_{oct2},

1 and ferryl terminations.[42] Full-potential density functional theory calculations by Zhu *et*

2 *al.*[43] show that the Fe_{oct2} termination is energetically more favorable using a local

3 density approximation (LDA)+*U* approach; their result is consistent with that from *ab*

4 *initio* periodic Hartree-Fock (HF) calculations,[44] although   HF bulk band-structure

5 calculations fail to reproduce the known antiferromagnetic alignment of magnetic

6 moments within the tetrahedral and octahedral sublattices.[26]

7 STM and low-energy electron diffraction (LEED) intensity analysis at 1000 K in a 10^{-6}

8 mbar atmosphere indicates the Fe_3O_4 (111) surface forms an unreconstructed bulk

9 termination that exposes ¼ ML Fe_{tet1} atoms over a close-packed oxygen layer, with

10 protrusions arranged in a hexagonal lattice with a 6 Å periodicity.[45-46] Both Paul *et al.*[47]

11 and Shimizu *et al.*[48] report that the Fe_{tet1} termination is routinely observed in naturally

12 grown single crystals at room temperature whereas Fe_{oct2} appears only when the

13 sample is prepared under oxygen-poor conditions, for instance, when exposed to UHV

14 for a long period of time. This supports the results of GGA+*U* calculations by Grillo *et*

15 *al.*[49] and Kiejna *et al.*[50] where they found the two surfaces have comparable

16 thermodynamic stabilities at this limit. Another type of coexistence of surface

17 terminations has been observed by Berdunov *et al.*[51] Here the regular Fe_{tet1} termination

18 consists of the superstructure with an oxygen-rich surface for crystalline Fe_3O_4 (111)

19 possibly with oxygen vacancies after annealing in an oxygen partial pressure of 10^{-6}

20 mbar at 950 K and subsequently cooling to room temperature.

21 An alternative to bulk termination reconstruction is the existence of defects, *e.g.*,

22 vacancies or adatoms, on the surface. Lennie *et al.*[41] have proposed that the irregular

23 texture observed in their STM images indicates the presence of defects in the surface

8

1   layer. One of the possible defects is an iron vacancy formed on Fe_{oct1} termination to

2   stabilize the surface polarity. In the Fe_{oct1} surface, a single V_{Fe} is expected to be more

3   stabilizing than two cationic vacancies as its surface charge (+5) from the remaining

4   octahedral ions is closer to half the absolute value of the subsurface charge (-4), which

5   fulfills the condition for the cancellation of the macroscopic dipole moments according to

6   classical electrostatics.[22] Ferric iron vacancies have also been observed on Fe_{tet1}-

7   terminated epitaxial Fe_3O_4 (111) films grown on Pt (111) substrates in an 10^{-6} mbar

8   oxygen partial pressure,[46] as have inhomogeneities caused by FeO_x agglomerates[52]

9   and FeO_{1-x} overlayers[46-47] on the surface. In order to evaluate the impact of defects, in

10 addition to four bulk terminations in the [111] direction (Fe_{tet1}, Fe_{oct1}, Fe_{oct2}, and O_1), we

11 have chosen to study single cationic vacancies formed at the octahedrally-coordinated

12 iron layer (Fe_{oct1}) on the surface, as shown in Figure 2a. Iron vacancies in octahedral

13 sites are exceptionally noteworthy as they are associated with the oxidation redox

14 cycles of magnetite(100)[53] in contrast to oxygen vacancies in other metal oxides.[54] We

15 have also considered oxygen vacancies in the close-packed oxygen layer as proposed

16 in earlier STM studies.[51]

17 Other possible surface modifications are attachments of foreign atoms or ions from the

18 residual atmosphere due to experimental conditions. Several STM studies have

19 observed adsorbates above the atomic layer.[47, 52] Importantly, high-resolution STM

20 measurements show there is a distinctive step of 1.2±0.1Å above the regular Fe_{tet1}

21 terminated surface, depicted in Figure 2b, suggesting that surface iron atoms may be

22 capped by a single oxygen atom at the atop position.[42] A similar termination, with a

23 hydroxyl group on top of the surface terminating cations, has been proposed after water

9

1   exposure.[48, 55] The STM results indicate that dissociative water adsorption to form

2   surface hydroxyls takes place on a termination of Fe_3O_4 (111) thought to contain a 1/4

3   monolayer of Fe^{3+} ions on top of a close-packed oxygen monolayer.[56] To evaluate this

4   class of defects, we have modified the Fe_{tet1} termination with two adsorbates, an oxygen

5   atom and a hydroxyl group. Thus, in total, we will consider four defect-containing

6   surface terminations; (i) iron vacancy in Fe_{oct1} (V_{Fe}, Figure 2a); (ii) oxygen vacancy in O_1

7   (V_O); (iii) oxygen adatom on Fe_{tet1} (ferryl, Figure 2b); and (iv) hydroxyl adsorbate on the

8   Fe_{tet1} termination.

9

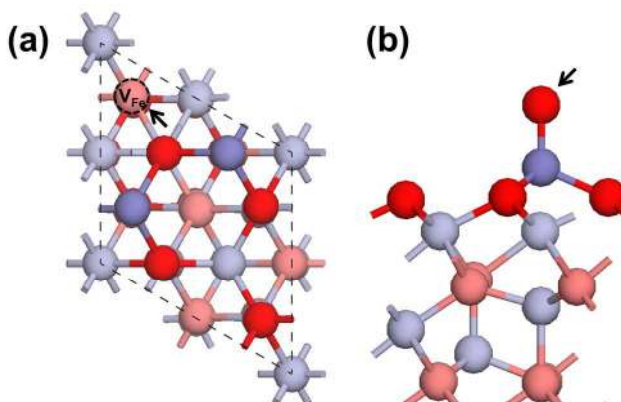10 **Figure 2 (a) Top view of the Fe_{oct1} termination with one Fe vacancy. The vacant site is**
11 **indicated with an arrow. (b) Side view of the Fe_{tet1} termination with ferryl group formation**
12 **upon attachment of an additional oxygen atom, indicated with an arrow, on the surface.**
13 **Fe atoms are colored blue, and oxygen ions are colored red.**

14

15 **b) Computational details**

16 First-principles calculations have been performed using spin-polarized DFT as

17 implemented in the Vienna *Ab initio* Simulation Package (VASP).[57-58] The ionic

18 potentials are described by the projector augmented wave (PAW) pseudopotential[59]

1   with valence configurations of $3d^7 4s^1$ and $2s^2 2p^4$ for Fe and O atoms, respectively. The

2   cutoff energy for the plane-wave basis set was chosen to be 550 eV.

3   On the basis of our previous theoretical study on the full electronic structure of cubic

4   Fe_3O_4,[60] we take the DFT+U approach[61] to modify the intra-atomic Coulomb interaction

5   among strongly correlated Fe $3d$ electrons. We consider the GGA exchange-correlation

6   functional of Perdew, Burke, and Ernzerhof (PBE).[62-63] The DFT+U method used here

7   is a simplified rotationally invariant formulation by Dudarev *et al.*[64] where the on-site

8   Coulomb parameter, U, and exchange parameter, J, are combined into a single

9   parameter, $U_{eff} \equiv U - J$. We applied U_{eff} = 4 eV for Fe $3d$ electrons in the calculations.

10 Brillouin-zone integration was performed on Monkhorst-Pack grids[65] with a $7 \times 7 \times 1$

11 mesh where a Gaussian-smearing approach with σ=0.05 eV is used during the ionic

12 optimization, while total energies and densities of states (DOS) were calculated using

13 the tetrahedron method with Blöch corrections.[66] Atomic charges were estimated within

14 the Bader scheme using converged FFT grids.[67-68] All of the vacancies and adatoms are

15 uncharged. Bulk properties for Fe_3O_4 were calculated using a unit cell containing 24 Fe

16 and 32 O atoms which was fully relaxed while preserving cubic symmetry. We found

17 that PBE+U successfully reproduced the electronic and magnetic properties of the bulk

18 Fe_3O_4 and describe the results from this methodology throughout our discussion. As the

19 energies calculated using different values of U cannot be compared, the value for U

20 must be transferrable amongst both the different multivalent oxides and metallic

21 systems. An alternative to the empirical U term is the use of hybrid functionals which

22 may provide a better treatment of exchange and correlation effects in both extended as

23 well as localized states. In our previous work on bulk magnetite,[60] we compared the

1   PBE+U results to those of both a conventional exchange correlation functional, PBE,

2   and a modified version of the range-separated hybrid functional, HSE06.[69-70] As the

3   optimal amount of Hartree-Fock (HF) exchange is system dependent, we utilized

4   HSE(15%), where the HF exchange mixing coefficient, a, was taken to be 0.15 and ω,

5   the parameter that defines the partitioning between the short- and long-range exchange

6   components, was 0.11 bohr^{-1}. A comparison to these other DFT approaches is

7   presented in the supporting information (SI). The effect of dispersion corrections was

8   examined for a subset of the systems studied, and they introduce only extremely small

9   changes in the electronic structure.

10 A well-established tool to investigate the electronic structure of surfaces and interfaces

11 at the DFT level is the repeated slab approach that allows one to take easy account of

12 the two-dimensional periodic character of such systems. The surface has been modeled

13 using a symmetric slab with of a (1×1) unit cell which is based on cubic-phase Fe_3O_4

14 (a= 8.488 Å). The slabs are separated by a vacuum space of approximately 20 Å. A top

15 view and side view of the stacking sequence are shown in Figure 1. The optimized

16 lattice vector within PBE+U[60] are slightly overestimated compared to the experimental

17 value (a=8.396).[71] PBE+U calculations provide a net magnetic moment of 3.99 μ$_B$/f.u.

18 compared to the experimental value of 4.05 μ$_B$/f.u..[72] In order to maintain bulk behavior

19 below the surface, the central layers were kept fixed at the bulk crystal positions during

20 the structural optimization while the outermost six layers on both sides of the slab were

21 allowed to relax. The ion positions were optimized using a conjugate-gradient algorithm

22 until the Hellmann-Feynman forces were less than 0.01 eV/Å and energy convergence

23 was reached within 10^{-5} eV/atom. An antiferromagnetic ordering, where the sign of the

12

1   Fe_{oct} atoms are antiparallel to those on the Fe_{tet} atoms, was taken as the initial magnetic

2   configuration and allowed to relax for all the surface models. The surface energy,

3   atomic charge, magnetic moment, and relaxation pattern were analyzed using a series

4   of Fe_{tet1} terminations with different stoichiometry by changing the slab thickness and the

5   results are shown in Table S1 in SI. The data presented in the text are for slabs

6   consisting of more than 17 layers where these surface characteristics have converged.

7   **c) Thermodynamic stability of surface terminations**

8   The stability of various surface terminations of iron oxides can be determined using a

9   simple thermodynamic approach. If the surface system is modeled in DFT by a slab with

10   two equivalent surfaces, the surface energy can be obtained by the following equation

11   where it is assumed that the Gibbs free energy (G) can be approximated by the

12   calculated internal energy (E):

$$\gamma = \frac{1}{2A}(E_{slab} - E_{bulk}) \tag{1}$$

14   In Equation 1, γ denotes the surface energy, A the surface area of the unit cell, E_{slab} the

15   total energy of the slab, and E_{bulk} the total energy of the bulk system with the same

16   number of atoms as in the slab: $E_{bulk} = N_{Fe}\mu_{Fe} + N_O\mu_O$; here, N_{Fe} and N_O represent the

17   numbers of each type of atoms while μ_{Fe} and μ_O denote the chemical potentials of a Fe

18   atom and an O atom. When there is enough bulk material to act as a thermodynamic

19   reservoir, the potentials of the components are no longer independent but are related by

20   the condition of thermal equilibrium in bulk Fe_3O_4:

$$3\mu_{Fe} + 4\mu_O = \mu_{Fe_3O_4} \tag{2}$$

13

1   where $\mu_{Fe_3O_4}$ is the DFT energy of bulk Fe_3O_4 per formula unit. This constraint can be

2   used to eliminate the dependence of the surface energy on μ_{Fe}. In this approximation

3   and at equilibrium, the surface energy can be expressed as a function of the oxygen

4   chemical potential as:

5
$$\gamma = \frac{1}{2A}\left[E_{slab} - \frac{1}{3}N_{Fe}\mu_{Fe_3O_4} + \left(\frac{4}{3}N_{Fe} - N_O\right)\mu_O\right] \tag{3}$$

6   In this way, it is possible to determine the relative stabilities of slabs with different

7   stoichiometries.

8   The oxygen chemical potential varies with its partial pressure (p) and temperature (T):

9
$$\mu_O(T,p) = \mu_O(T,p^\circ) + 1/2 k_B T \ln\left(\frac{p}{p^\circ}\right) \tag{4}$$

10   where p° is the pressure in the reference state and k_B, the Boltzmann constant. As

11   experimental conditions have a considerable impact on the oxygen chemical potential, it

12   is necessary to evaluate the surface energies for various surface terminations as a

13   function of the chemical potential of oxygen to determine the surface stability in a given

14   environment. For example, the oxygen chemical potential at p =10^{-6} mbar and T =900 K,

15   one of the typical conditions for annealing of magnetite,[23] is calculated to be -1.78 eV

16   with the $\mu_O(T,p)$ reference state defined as the total energy of molecular oxygen at the

17   standard pressure, p° =1 bar.[73] It is useful to restrict the range of oxygen chemical

18   potentials by considering the limiting conditions. The oxygen-rich limit can be defined as

19   the chemical state in which molecular oxygen starts to condense on the surface. By

14

1   assuming that such condensed oxygen is in equilibrium with gas-phase oxygen, the

2   upper limit of the oxygen chemical potential becomes:

$$\mu_O(T,p) = \frac{1}{2} E_{O_2} \tag{5}$$

4   where E_{O_2} is the DFT energy of an O_2 molecule.

5   At the oxygen-poor limit, reduction of the oxide from magnetite to wüstite (FeO) and

6   further to metallic iron occurs. Thus, a reasonable minimum μ_O corresponds to the

7   condition where Fe crystallizes and oxygen separates onto the surface according to the

8   equilibrium of bulk magnetite, that is:

$$\mu_O = \frac{1}{4}(\mu_{Fe_3O_4} - 3\mu_{Fe,bulk}) \tag{6}$$

10   where $\mu_{Fe,bulk}$ is the DFT-calculated chemical potential of metallic Fe.

11   **III. Results and Discussion**

12   We have selectively calculated four bulk terminations in the [111] direction; Fe_{tet1}, Fe_{oct1},

13   O_1, Fe_{oct2}, omitting the Fe_{tet2} and O_2 surfaces that were reported to be highly unstable.[31]

14   While it must be emphasized that the bulk-terminations have been examined

15   previously,[49-50] it is important to include a breif discussion here in order to illustrate the

16   large differences between these surfaces and the four modified surfaces incorporating

17   surface defects (iron vacancy in Fe_{oct1}, oxygen vacancy in O_1; oxygen adatom (ferryl)

18   and hydroxyl adsorbate on the bulk Fe_{tet1} termination). Below, we will turn successively

19   to a discussion of: surface stability, ionic relaxation, surface electronic structure and

20   chemistry, and spin polarization near the Fermi level for each of these surface models.

1

2   **a) Surface stability**

3   Using Equation 3, we have evaluated the relative stabilities of the surface models. The

4   results are plotted as a function of oxygen partial pressure in Figure 3 for the PBE+U

5   functional. Previous theoretical studies containing only bulk terminations have

6   concluded that the Fe_{tet1} termination has the lowest surface energy in the oxygen-rich

7   regime, while the Fe_{oct2} and Fe_{oct1} surfaces are competitive in the oxygen-poor regime.[39,]

8   [49-50, 74] The defect-containing surfaces that we examine here are viable in comparison to

9   the bulk-like terminations. For example, as both the V_O and ferryl-terminated surfaces

10   are within 100 meV/Å^2 (1.60 J/m^2) of the Fe_{tet1} surface near the oxygen-rich limit,

11   specific sample preparation methods or environmental conditions may lead to the

12   observation of these oxygen-rich surfaces. The ferryl termination is more stable than the

13   formally oxygen-terminated surfaces over most of the pressure range. Experimental

14   observations by Berdunov *et al.*[51] indicate the presence of such oxygen-terminated

15   surfaces, which are higher in surface energy than the defect-containing surfaces. This is

16   in agreement with the calculated large binding energy of an oxygen atom located on a

17   bridge position between Fe_{tet1} and Fe_{oct2} atoms by Santos-Carballal *et al.*[74] We note that

18   there is a well-known overbinding problem[75] in small molecules within DFT (and

19   DFT+U), which can lead to an inaccurate energy for molecular oxygen. If we replace the

20   calculated binding energy of oxygen gas with the experimental value, 5.23 eV[76] ($E_{B,exp.}$),

21   the chemical potential limit can be rewritten as $\mu_{O_2,exp} = E_{B,exp.} + 2\mu_{O,DFT}$. This equates

22   to shifting the oxygen-rich limit to a more positive value by 0.4 eV, shown as the

23   rightmost vertical line in Figure 3. This is smaller than the 1.36 eV shift determined by

1   differences in experimental and calculated formation energies over a series of oxides,

2   which was used previously.[77] At this extreme, the ferryl termination becomes

3   isoenergetic with the Fe_{tet1} termination.

4   In the oxygen-poor limit, the Fe_{oct2} termination is shown to be more stable than the Fe_{tet1}

5   termination, as suggested before.[41, 47-48] The Fe_{oct1} termination becomes more

6   energetically favored than the Fe_{oct2} termination only at extremely low oxygen chemical

7   potentials, beyond the estimated oxygen-poor limit, because of the higher density of Fe

8   ions on the Fe_{oct1} surface. However, missing Fe atoms on this termination, labeled as

9   V_{Fe}, moderately stabilize the surface, leading to competitive surface energies with the

10   Fe_{oct2} termination over the entire range of oxygen chemical potentials.

11   The sensitivity of our results to choice of functional is presented in Figure S1 of the SI.

12   Despite the limitation of using a constant empirical U correction for both the oxide and

13   the metallic species, this method reproduces the enthalpy of formation for binary-

14   manganese oxides within 4%.[78] Additional quantitative accuracy could be obtained by

15   utilizing a method systematically combining GGA and GGA+U energies (however,

16   further experimental data would then be required[79]). In general, such additional

17   numerical accuracy is not needed as the surface stabilities using different functionals

18   show the same ordering as the PBE+U method but with *further* stabilization of the ferryl

19   termination. The hydroxyl surface is also dependent on the hydrogen (or water) partial

20   pressure and is not plotted in Figure 3. However, the observation of hydroxyl groups on

21   epitaxial Fe_3O_4 (001) surfaces[80] indicate that this termination can appear not only in

22   humid conditions,[81] but is competitive in ultrahigh-vacuum environments.
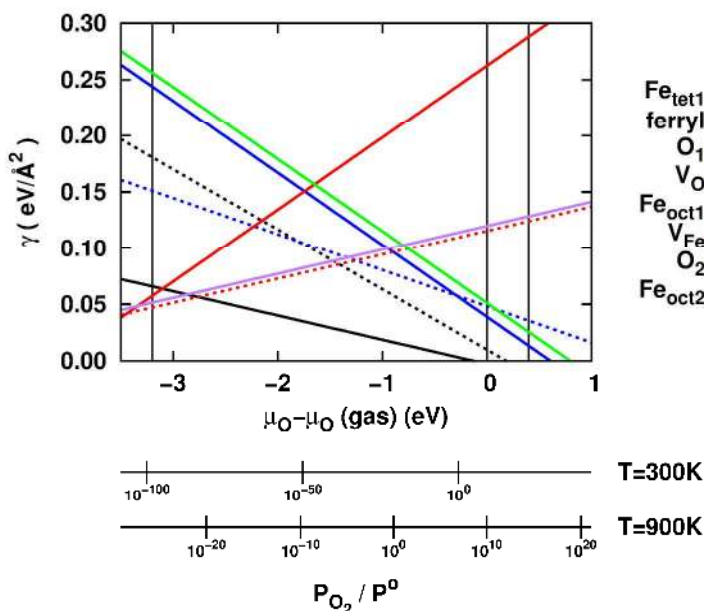
1

2 **Figure 3 PBE+*U* derived surface energies of the different terminations plotted against the**
3 **oxygen chemical potential. The vertical black lines indicate the allowed range of the**
4 **chemical potential. The bottom two horizontal axes indicate corresponding oxygen**
5 **pressure in log scale at 300 K and 900 K, respectively (p° = 1 bar).**

6

7 The modified surfaces presented above are high in defect density, with one defect or

8 adlayer in each unit cell. The stability of the ferryl surface with a lower defect coverage

9 on the Fe_{tet1} termination ($\Theta = 1/4$) is shown in Figure 4. This approach has previously

10 been used to study mixed terminations of hematite surfaces.[82] The resulting mixed

11 surface is nearly equal in energy to the Fe_{tet1} termination over much of the potential

12 range, and the point at which it becomes lower in energy shifts further toward lower

13 oxygen chemical potentials. In a macroscopic surface, these defects may be present,

14 even if higher in energy in a small unit cell. Given the stringent requirements for spin-

15 injection and detection in devices, contributions from these slightly higher-energy

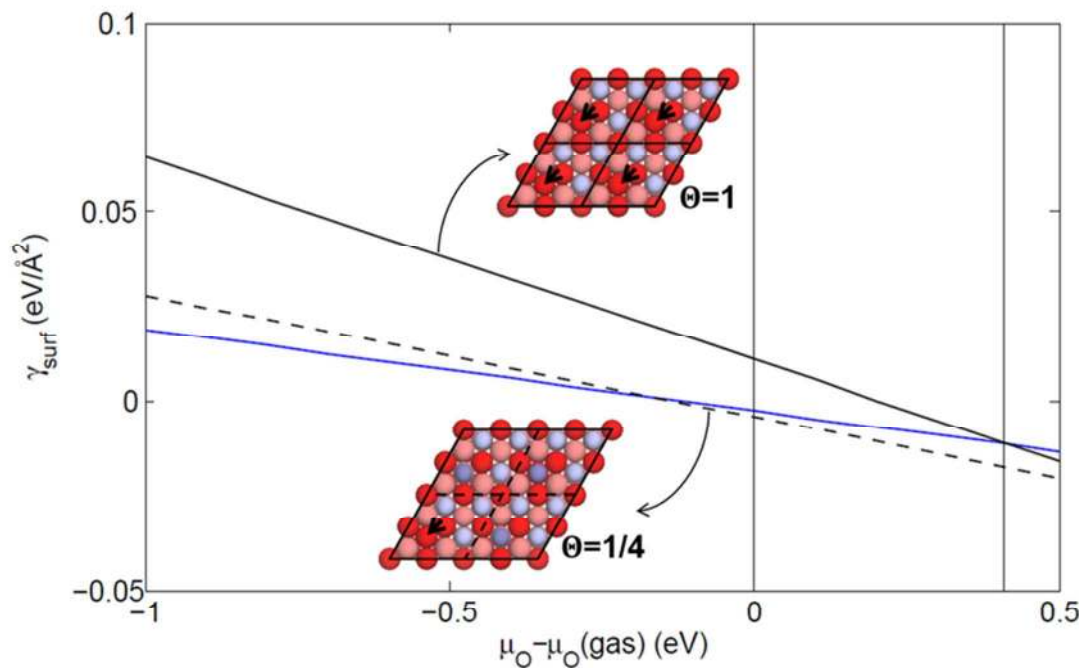16 surfaces may determine the overall success of a device.

1

Figure 4 Surface free energy change as a function of the oxygen chemical potential for two different ferryl concentrations on the surface: 25% (dotted black) and 100%. (solid black) The blue line indicates Fe_{tet1} termination. The arrows in inset images correspond to the positions where oxygen adatoms are attached.

b) Ionic relaxation

As described above, (111) surfaces created from cleavage of bulk cubic magnetite are unstable as two inequivalent layers of opposite charge densities alternate perpendicular to the surface. A high dipole moment, 29.5 D, is estimated within the repeat unit of six distinct layers when using formal charges and the bulk interlayer spacing.[22] One pattern of stabilization of these surfaces is through significant changes in the nuclear positions of the atoms comprising the surface layers.

The interlayer relaxations are determined mostly by a response to the large dipole moments of alternating polar layers in the surface layers. The relaxations between

1 adjacent layers (ij) of the outmost six layers as a percentage (Δ_{ij}) of the bulk interlayer

2 distance are shown in Figure 5 for terminations based on (a) Fe_{tet1}, (b) O_1, and (c) Fe_{oct1}.

3 For instance, in the Fe_{tet1} termination, the surface Fe_{tet1} atom shows a strong inward

4 relaxation and the interlayer spacing between the surface layer and subsurface layer

5 decreases by 37%. Further reduction in polarity is achieved by a 22% compression in

6 the O_1- Fe_{oct1} distance, which fully stabilizes the surface as there are progressively

7 smaller changes in geometries for the rest of the slab. The overall relaxation of the

8 Fe_{tet1} termination is consistent with a previous LEED analysis.[45] For the ferryl and

9 hydroxyl surfaces, the surface Fe_{tet} atom retains its bulk-like tetrahedral coordination by

10 binding to the oxygen adatom; also, the electrostatic attraction of a surface Fe ion to the

11 oxygen atoms in the sublayer is balanced by the adatom. The newly formed Fe=O and

12 Fe-O bonds are estimated to be 1.62 Å and 1.77 Å, which are consistent with the 1.5 Å-

13 height adsorbates reported in STM studies.[52] Hence, the Fe_{tet1}-O_1 distance decreases

14 by 17% and 9% for the ferryl and hydroxyl surfaces. However, the relaxations in the

15 next layers in the slab are now in the opposite direction than in the Fe_{tet1} slab, with the

16 Fe_{oct1}-O_2 distance being compressed and the O_2-Fe_{tet2} distance slightly expanding.
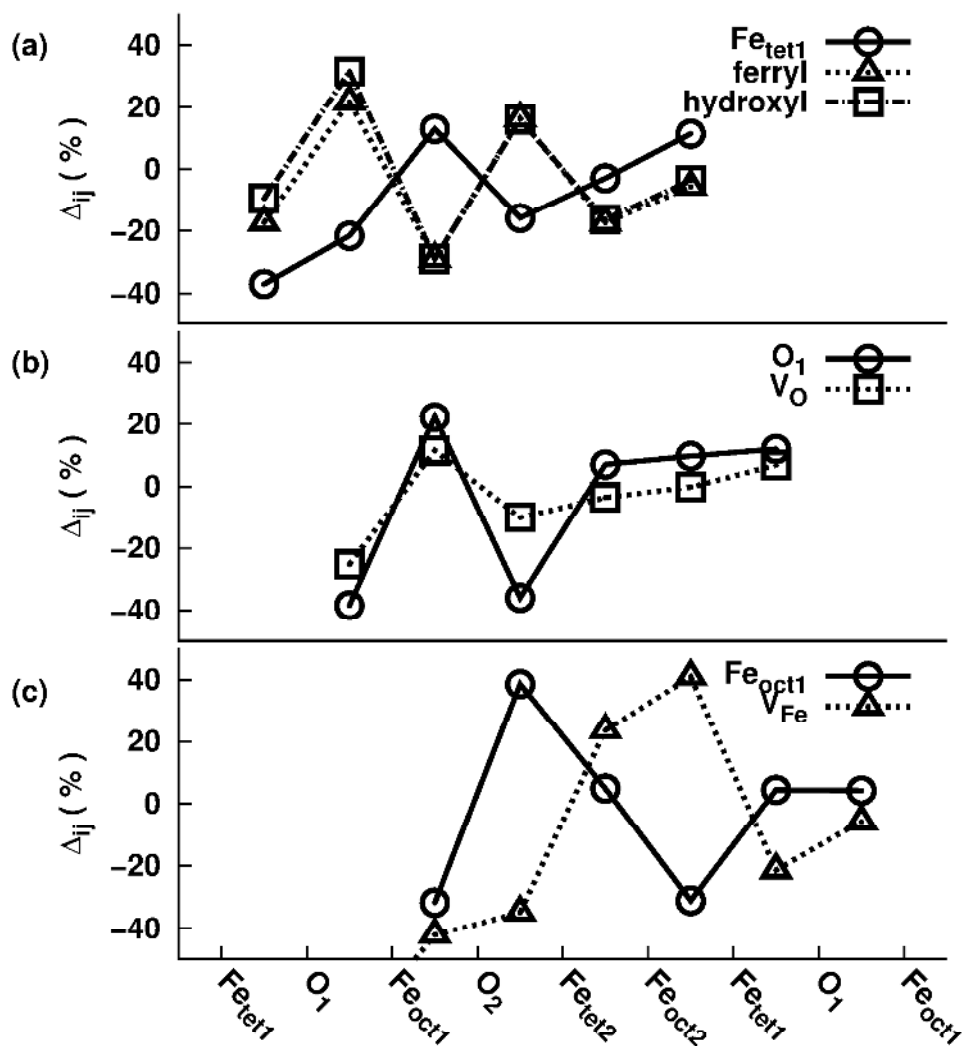
Figure 5. Surface relaxations in the outmost six layers given as a percentage (Δ_{ij}) of the bulk interlayer distances between two adjacent surface planes (i) and (j) projected onto the c axis for the seven terminations of Fe_3O_4 (111). Terminations based on (a) Fe_{tet1}, (b) O_1, and (c) Fe_{oct1} are shown in separate panels. The bulk interlayer distances between Fe_{oct1}-O, Fe_{tet}-O, and Fe_{tet}-Fe_{oct2} are 1.19 Å, 0.64 Å, and 0.61Å, respectively.

There are only moderate changes in interlayer spacing in the O_1 surface, and these are smaller in the V_O surface due to the reduced surface charge. The introduction of a Fe vacancy in the Fe_{oct1} termination (V_{Fe}), shown in 5c, changes the local geometries at the surface, although in a different fashion from the bulk Fe_{oct1} termination. In the V_{Fe} termination, one of the four oxygen atoms in the subsurface ends up migrating above

1   the iron surface due to the vacated volume and a strong electrostatic attraction between

2   two outermost layers. As a consequence, the surface Fe_{oct1} atoms bind more strongly to

3   the surrounding oxygen atoms with a reduced bond length, 1.88 Å, compared to the

4   bond in the Fe_{oct1} termination, 1.93 Å. Moreover, three remaining oxygen atoms in the

5   O_2 layer are allowed to fairly interact with the underneath iron layers, Fe_{tet2} and Fe_{oct2},

6   since the protruding oxygen exclusively forms ionic bonds with the two Fe atoms on the

7   surface.

8   **c) Surface electronic structure and chemistry**

9   Since the surfaces are created by cleaving ionic bonds, significant charge redistribution

10   occurs due to the appearance of dangling bonds. In this study, density of states (DOS),

11   Bader charge, net magnetic moment, and work function are calculated to describe the

12   related stabilization mechanism upon surface cleavage and change in surface chemistry.

13

14   **Density of states**

15   The DOS projected on Fe_{oct}, Fe_{tet}, and O atoms for near-surface (3-4) layers of each

16   termination are displayed in Figure 6. The electronic structure of bulk Fe_3O_4 in a cubic

17   $Fd\bar{3}m$ phase, shown in the SI (Figure S2), can be described as a half-metallic oxide,

18   which is consistent with the crystal-field splitting explanation for the octahedral Fe ions

19   that the fivefold d levels separate into three degenerate t_{2g} levels and two degenerate e_g

20   levels.[60] The PDOS for the central layers of the slab retain this electronic structure.

21   The PDOS for the surface layers in the Fe_{tet1} termination, plotted in Figure 6a, show that

22   the minority (spin-down) Fe t_{2g} states from the octahedral sites are no longer present at

1   or near the Fermi level and there appears a surface state related to tetrahedral-site iron

2   in the middle of the majority spin (spin-up) gap. The partial charge density for this state

3   is shown in Figure 6d, and demonstrates that the $3d$ orbitals in the direction of reduced

4   coordination, *i.e.*, the [111] direction, are more stabilized and now lie below the Fermi

5   level. In general, surface truncation of iron-terminated surfaces promotes a further

6   splitting within Fe_{tet1} e_g and t_{2g} orbitals at the surface as the symmetry is lowered

7   because of missing apical oxygen.[83] Since the Fe_{tet1} termination has a positively

8   charged surface, the top Fe_{tet1} layer obtains more electrons through electronic

9   redistribution to reduce the polarity, with the bottom of the conduction band becoming

10   occupied. The ferryl termination, where the Fe_{tet1} surface has an additional oxygen atom

11   bound to the exposed iron atom, shows a different DOS with respect to the Fe_{tet1}

12   surface; the ferryl group comprises a set of states near the Fermi level and the surface

13   state related to tetrahedral-site iron no longer appears in the spin-up gap (the PDOS of

14   adsorbate oxygen is colored in magenta in Figure 6). In the hydroxyl termination these

15   hybridized states are stabilized and now located in the same region as the surface

16   oxygen atoms. In the O_1 subsurface, oxygen $2p$-derived states still have a strong

17   dispersion between -1 eV to -6 eV. Compared to bulk states, they are shifted to higher

18   binding energy by ~ 1 eV in response to the lowered coordination upon surface
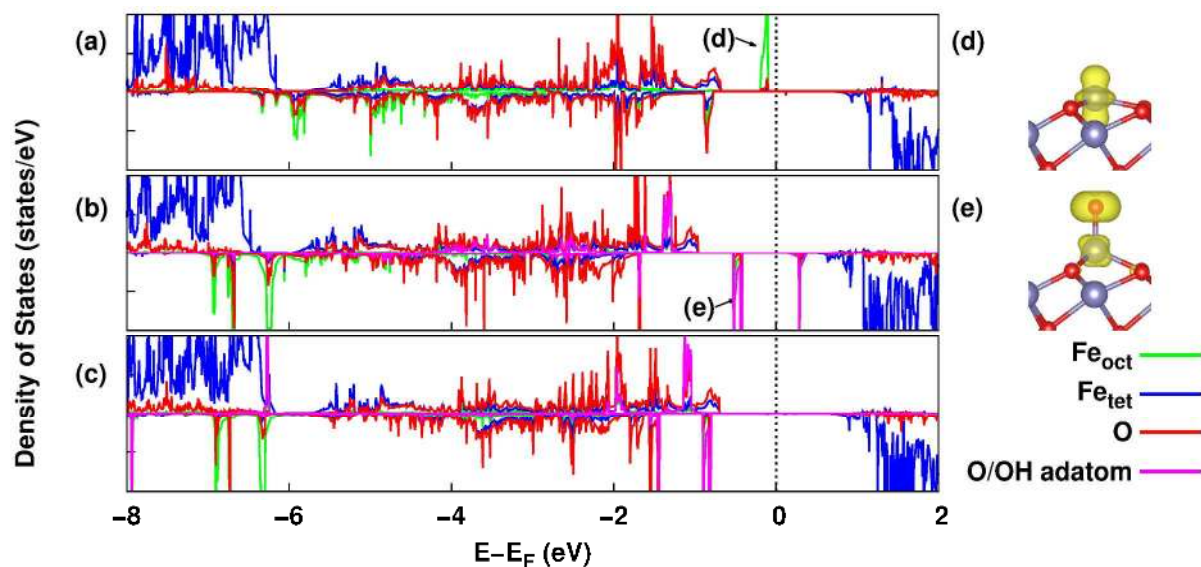
19   cleavage.

Figure 6. Electronic densities of states of near-surface (3-4) layers for the surfaces: (a) Fe_{tet1},(b) ferryl, and (c) hydroxyl terminations from PBE+U calculations from -8 eV below to +2 eV above the Fermi level. The Fermi level (= zero of energy, see text) is indicated with a dashed line. Partial charge densities of the surface states marked with short arrows for (d) Fe_{tet1} and (e) ferryl terminations. PDOS from Fe_{tet1} atoms are blue, Fe_{oct} atoms are green and lattice oxygen atoms are red.

In the Fe_{oct1} termination with a vacancy, V_{Fe}, there are no longer octahedral states observed around the Fermi energy in contrast to Fe_{oct2} (see Figure S2 in SI) although the two models have the same Fe coverage over the oxygen sublayer, *i.e.*, ½ ML. Instead, the electrons are redistributed over the surface in a fashion similar to the Fe_{oct1} termination. In both cases, the Fe 3d states on octahedral sites are shifted to lower energy, leading to a reduction of these Fe atoms to stabilize the positively charged outmost layer. The occupied Fe 3d minority spin states (between -1 eV and -0.5 eV) are more populated in the bulk-terminated Fe_{oct1} surface. Despite overall similarity in the PDOS between Fe_{oct1} and V_{Fe}, the states just below the Fermi-level (marked with arrows c and d in Figure 7) are qualitatively different. In the Fe_{oct1} surface the charge is

1   delocalized over the first layer of the surface, whereas the iron vacancy leads to the

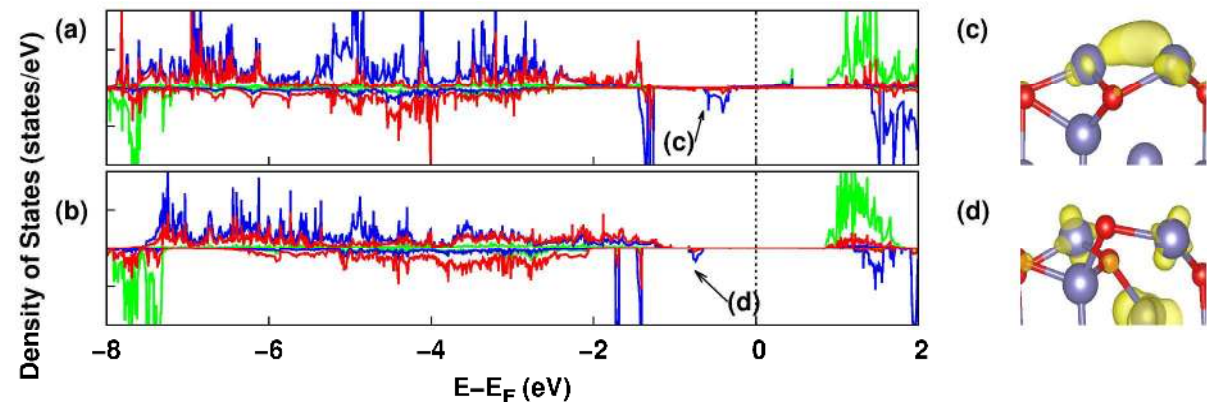2   state becoming more localized on each Fe atom on the surface.

4   **Figure 7. Electronic densities of states of near-surface (3-4) layers for the surfaces: (a)**
5   **Fe_{oct1},(b) and (b) V_{Fe} terminations from PBE+U calculations from -8 eV below to +2 eV**
6   **above the Fermi level. The Fermi level (= zero of energy, see text) is indicated with a**
7   **dashed line. Partial charge densities of the surface states marked with short arrows for (c)**
8   **Fe_{oct1} and (d) V_{Fe} terminations. PDOS from Fe_{tet1} atoms are blue, Fe_{oct} atoms are green**
9   **and lattice oxygen atoms are red.**

11   For the O_1 termination, the surface also tends to be oxidized due to the highly

12   negatively charged surface layer. Hence, the O 2p states which comprise the valence

13   band in the bulk shift above the Fermi level, leading some of these states to become

14   unoccupied upon cleavage. The V_O surface shows the similar results. The DOS for

15   these surfaces are shown in the section S5 of SI.

17   **Bader charge and net magnetic moment**

18   The ionic and electronic relaxations described above can also be understood through

19   changes in Bader charge and magnetic moment on each of the atoms when going from

20   bulk to the surface, as presented in Table 1. The atomic charges for the bulk cubic

1 system show that all the equivalent octahedral ions with a formal oxidation state of +2.5

2 have a Bader charge of +1.72 |e| and the tetrahedral ferric sites, a charge of +1.86 |e|.

3 The oxygen ions each have a charge of -1.33 |e|. In general, the charges of both Fe and

4 O tend to decrease in absolute values compared to the bulk due to reduced

5 coordination of surface atoms and electronic redistribution. We present the results of

6 four terminations in Table 1. The hydroxyl surface has a similar charge and spin

7 distribution as the ferryl surface. As with the surface relaxations and DOS, there is little

8 change between the O_1 and V_O terminations.

9 **Table 1. Average change in atomic charge and magnetization (per atom) in the top layers**
10 **for four terminations. All the values listed represent the changes from the values for the**
11 **equivalent atoms in the bulk system. Net magnetic moment for bulk Fe_{oct}, Fe_{tet}, and O**
12 **atom are 3.96-3.98, 4.09, and 0.03 μ_B, respectively. The experimental magnetic moment**
13 **for bulk Fe_{tet} is 3.82 μ_B.[84] [a]Values from the PW91+U (U_{eff} = 3.61 eV) calculations of ref. 50.**

Fe_{tet1}				ferryl		
layer	Δq (e)	Δμ (μ_B)		layer	Δq (e)	Δμ (μ_B)
				O	-0.66	-0.12
Fe_{tet1}	+0.41	-0.54(-0.53[a])		Fe_{tet1}	-0.04	-0.83
O_1	-0.07	+0.22		O_1	-0.10	+0.21
Fe_{oct1}	-0.19	+0.22		Fe_{oct1}	-0.20	+0.22
O_2	-0.04	+0.04		O_2	-0.04	+0.04

Fe_{oct1}				V_{Fe}		
layer	Δq (e)	Δμ (μ_B)		layer	Δq (e)	Δμ (μ_B)
Fe_{oct1}	+0.60	-0.46		Fe_{oct1}	+0.35	-0.37
O_2	+0.03	-0.01		O_2	-0.03	-0.05
Fe_{tet2}	+0.02	-0.04		Fe_{tet2}	+0.05	-0.04
Fe_{oct2}	+0.24	-0.30		Fe_{oct2}	+0.25	-0.33

14

15 Due to the dangling bonds, the top layer in the Fe_{tet1} termination gains 0.41 electrons,

16 as anticipated from the change in the DOS that the originally unoccupied conduction

17 band of the spin-up channel is slightly shifted below the Fermi level. The oxygen ions in

18 the second layer also help reduction of the surface dipole by losing 0.07 electrons to be

1   less negative, which contributes to further stabilization. Meanwhile, each of the three

2   iron ions in the third layer becomes more positive by 0.19 |e|, which alleviates the

3   overall negatively charged nature of the surface and subsurface. In the ferryl termination,

4   *i.e.*, when adding an atop oxygen to the exposed Fe_{tet1} atom, the charge on the Fe_{tet1}

5   atoms remain close to the bulk value. Just as in the Fe_{tet1} surface, there is an increase

6   in positive charge character for Fe_{oct1} in the third layer.

7   In the Fe_{oct1} and V_{Fe} terminations, there are essentially more electrons residing on the

8   topmost layer than in the bulk system. These electrons reduce the positive charge on

9   the iron atoms on the surface, although the O_2 sublayer preserves its bulk charge state.

10   Notably, in the V_{Fe} termination, the cationic vacancy brings about a lesser electron gain

11   to the remaining two surface Fe_{oct1} atoms.

12   The variations in magnetic moment of the surface atoms are consistent with the

13   changes in atomic charge, especially for the metal-terminated surfaces. For the ferryl

14   group, there is a decrease in magnetic moment of -0.83 μ_B for the Fe_{tet1} atom despite a

15   negligible variation in atomic charge, 0.04 e; this is the result of combined effects due to

16   depopulation of the originally occupied spin-up Fe_{tet} 3d orbitals in the valence band and

17   population of the previously unoccupied spin-down Fe_{tet} 3d orbitals, which is related to

18   bonding with the atop oxygen atom.

19   In the top two iron layers of Fe_{oct2} termination, see Table S3, the Fe_{oct} atoms gain

20   electron density in the bulk unoccupied minority spin (spin-down) bands, which leads to

21   a magnetic moment decrease. This is also the case for the Fe_{tet1}, Fe_{oct1}, and V_{Fe}

1   terminations; this result is reasonable as the Fe 3d orbitals in the minority spin states

2   are now more partially occupied while the majority bands stay fully occupied.

3

4   **Work function**

5   The work function is one of the critical surface parameters and is illustrative of the

6   charge distribution over the surface of a material. The work function, Φ, of a surface in

7   the DFT-slab framework is defined as:

$$\Phi = E_{vac} - E_f \qquad (7)$$

9   where E_{vac} is the plane-averaged electrostatic potential energy of an electron in the

10 vacuum region away from the slab surface at the distance where the potential energy

11 has reached its asymptotic value, and E_f denotes the Fermi energy of the total system.

12 Table 2 collects the work functions for each surface. The calculated work function of

13 5.76 eV for the model Fe$_{tet1}$ termination is 0.24 eV higher than the experimentally

14 measured value, 5.52 eV, for the same surface.[23] The value that we calculate for the

15 Fe$_{tet1}$ surface is 0.28 eV higher than the values from PW91+U (U$_{eff}$ = 3.61 eV)

16 calculations in ref. 50 and 0.15 eV and 0.75 eV lower than the O$_1$ and Fe$_{oct2}$ value,

17 respectively. The other three iron-terminated surfaces have lower work functions by up

18 to 2.61 eV whereas the oxygen-terminated surfaces, ferryl and O$_1$, show a narrow range

19 (0.33 eV) of work functions. Thus, there is a large difference between the calculated

20 work functions of the iron- and oxygen-terminated surfaces, which can be explained on

21 the basis of simple electrostatics: Magnetite has a dipole moment in the [111] direction

1   generated by alternating cation layers and anion layers; when the termination ends with

2   a negatively charged layer, the corresponding potential increases at the surface, which

3   gives rise to a relatively high vacuum level, while positively top charged layers give rise

4   to the opposite effect.

5   **Table 2. Work function is calculated for the eight surface terminations. [a]Value from the**
6   **PW91+U (U_{eff} = 3.61 eV) calculations of ref. 50.**

Surface	Termination	Work function (eV)
Fe_{oct1}	$^3/_4$ML Fe_{oct}	3.91
V_{Fe}	$^2/_4$ML Fe_{oct}	4.03
Fe_{oct2}	$^2/_4$ML (Fe_{oct}+Fe_{tet})	3.15 (3.90)[a]
Fe_{tet1}	$^1/_4$ML Fe_{tet}	5.76 (5.48)[a]
hydroxyl	$^1/_4$ML Fe_{tet}+OH	5.80
ferryl	$^1/_4$ML Fe_{tet}+O	7.61
V_O	$^3/_4$ML O	7.33
O_1	1ML O	7.94 (8.09)[a]
Exp.[23]	$^1/_4$ML Fe_{tet}	5.52

7

8   The work function decreases by 2.6 eV upon an increase in iron density over the

9   oxygen layer from 1/4 ML (Fe_{tet1}) to 2/4 ML (Fe_{oct2}). When introducing a Fe cation

10 vacancy on the Fe_{oct1} termination, the work function increases by +0.11 eV compared to

11 the bulk-terminated Fe_{oct1} surface (3.91 eV). This small change in work function

12 between Fe_{oct1} and V_{Fe} can be attributed to the charge states of the Fe_{oct} atoms

13 becoming more positive, from +1.12 |e| to +1.37 |e|, in the presence of the defect. The

14 work function for Fe_{oct2} is also smaller than the work function of the V_{Fe} termination with

15 exactly the same iron coverage at the surface. Given that the exposed surface cations

16 of Fe_{oct2} (+1.33 |e|) are as positive as in the V_{Fe} surface, the oxygen atom above the V_{Fe}

1   surface plays a substantial role in determining the work function difference of 0.88 eV

2   between the two surfaces.

3   In the ferryl termination, the negatively charged oxygen atoms on the top of the Fe

4   atoms bring about a substantial increase of 1.85 eV in work function compared to the

5   bulk-terminated Fe_{tet1} surface. Despite having a significantly less dense oxygen layer,

6   the work function of the ferryl termination then is comparable to that of the oxygen-

7   terminated surfaces, O_1 and V_O. An explanation for this behavior is the bond dipole

8   formed between iron and oxygen, which leads to a large dipole component in the

9   direction perpendicular to the surface. In the bulk oxygen terminations, the Fe-O bonds

10   are aligned at an angle to the surface, reducing the component perpendicular to the

11   surface. Thus, the atop oxygen on Fe_{tet1} plays a significant role in considerably

12   increasing the work function despite having a smaller negative charge than the oxygen

13   atoms on other terminations. This impact is diminished by the additional hydrogen in the

14   hydroxyl group. Finally, we note that while there is some quantitative variation

15   depending on the choice of methodology (shown in Figure S3), *e.g.*, the work function

16   varies up to 1.53 eV for the O_1 surface between PBE and HSE(15%), however, the

17   overall trends upon terminations are similar compared to the results from PBE+*U*.

18   **d) Surface chemistry**

19   As a consequence of atomic displacements and charge redistributions, the surfaces can

20   have quite different chemistries compared to those predicted from the bulk properties; in

21   addition, defect-modified surfaces can be different than bulk-terminated surfaces. An

22   example is depicted in Figure 8, which illustrates the electrostatic potential profile

23   measured at 1.3 Å, a typical bonding distance, above from the surface atoms for the

1   Fe$_{oct1}$ and V$_{Fe}$ terminations. Here, the octahedral Fe positions are distinguishable

2   because of their lower potential, displayed in blue. Combined with the Bader charge

3   analysis, it is clear that Fe$_{oct1}$ and V$_{Fe}$ are markedly different surfaces given the fact that

4   in the latter the positive charge near the iron atoms is intensified and the oxygen

5   protrusion contains a slight negative charge, in comparison to the bulk-truncated

6   surface. Thus, it is important to emphasize that the mode of chemisorption of an organic

7   layer, for instance, the binding of a phosphonic acid as was done on the (La,Sr)MnO$_3$

8   (LSMO) surface,[85] could be significantly different on a vacancy-containing surface

9   compared to a bulk termination. This change in mode of chemisorption would be

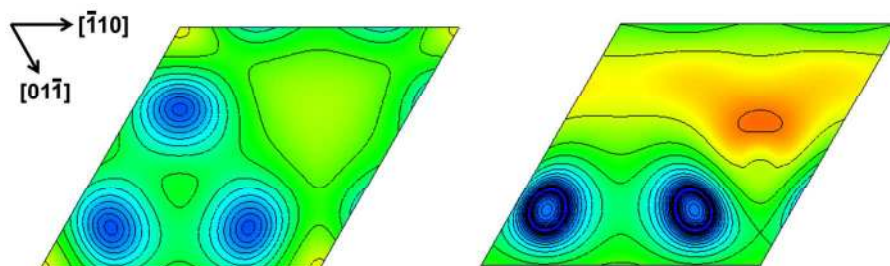10   significant in the performance of SAM-based magnetic tunnel junctions.

11

12

13   **Figure 8. Planar electrostatic potential plot evaluated at 1.3 Å above the Fe$_{oct1}$ atoms for**
14   **the Fe$_{oct1}$ (left) and V$_{Fe}$ (right) termination. The potential is illustrated in the reverse**
15   **rainbow spectrum: lower potential in the blue region and higher potential in the red**
16   **region.**

17

18   **e) Spin polarization near the Fermi level**

19   The spin polarization at the surface is a major factor determining the spin-injection and -

20   collection efficiency of an electrode. The spin polarization ratio at the Fermi level can be

1   defined as $P(E_f) = (n_\uparrow - n_\downarrow)/(n_\uparrow + n_\downarrow)$ where $n_\uparrow$ and $n_\downarrow$ are the densities at E_f of the

2   majority and minority spins, respectively. Dedkov *et al.*[86] measured $P(E_f)$ to be -80±5%

3   at room temperature near the surface of epitaxial Fe_3O_4 (111) films on Fe (110) using

4   spin-resolved photoemission spectroscopy. They attributed the high spin polarization to

5   the bulk Fe_3O_4 with a small reduction from the ideal value, -100%, due to the excitation

6   of spin waves at the surface. The half-metallic state of Fe_3O_4 is retained even after high

7   oxygen exposure as the spin-down electrons retain a high density-of-states near E_f

8   contrary to spin-up electrons. In contrast to those results, Pratt *et al.*[87] reported the

9   opposite spin polarity using the naturally-grown single crystal annealed under <10^{-8} bar

10   at 550 °C and proposed $P(E_f)$ of >20% measured using a spin-polarized metastable

11   helium beam [He(2^3S)] under magnetic fields up to 4 T at 298K. To reconcile these data,

12   the authors assigned the difference to the penetration depth of their probe beams,

13   which is much lower in the latter study than in UV photoemission where the octahedrally

14   coordinated Fe layers below the surface can contribute to the cumulative spin

15   polarization. This is also confirmed in the present study based on the quantitative

16   evaluation of layer resolved spin polarity, as illustrated in Section S7. A comparison of

17   the functional dependence of the cumulative layer polarization is also given in Figure S5.

18   In Figure 9, the spin polarizations, P(E), calculated for the top six layers, *i.e.* one repeat

19   unit (corresponding to approximately 4.8 Å from the surface), are plotted for the eight

20   terminations. As seen above, the DOS have distinctive features depending on the

21   surface termination; these features are directly reflected in the surface spin polarization.

22   The Fe_{tet1} termination, panel a, shows a positive spin polarization below and negative

23   above the Fermi level. In contrast, the ferryl termination presents a negative spin

1   polarization on both sides of the Fermi energy; as seen in the DOS, the negative spin

2   polarity at E_f originates from Fe $3d$-O $2p$ hybridized orbitals of the newly formed Fe=O.

3   The negative spin polarization below the Fermi level is no longer evident in the hydroxyl

4   termination, as the spin-down states associated with the adatom are no longer in the

5   spin-up gap. The defect structure of the Fe_{tet1} termination could significantly decrease

6   the positive value of $P(E_f)$, expected from the bulk electronic structure. As the

7   magnitude and polarization of the PDOS of the Fe_{oct1} and V_{Fe} terminations are similar,

8    $P(E)$ presents a similar profile in the region of the Fermi level. In the Fe_{oct1} surface, the

9   polarization ratio becomes positive slightly above the Fermi level, which is not seen in

10   the V_{Fe} surface. The O_1 and V_O terminations have nearly +100% spin polarization from -
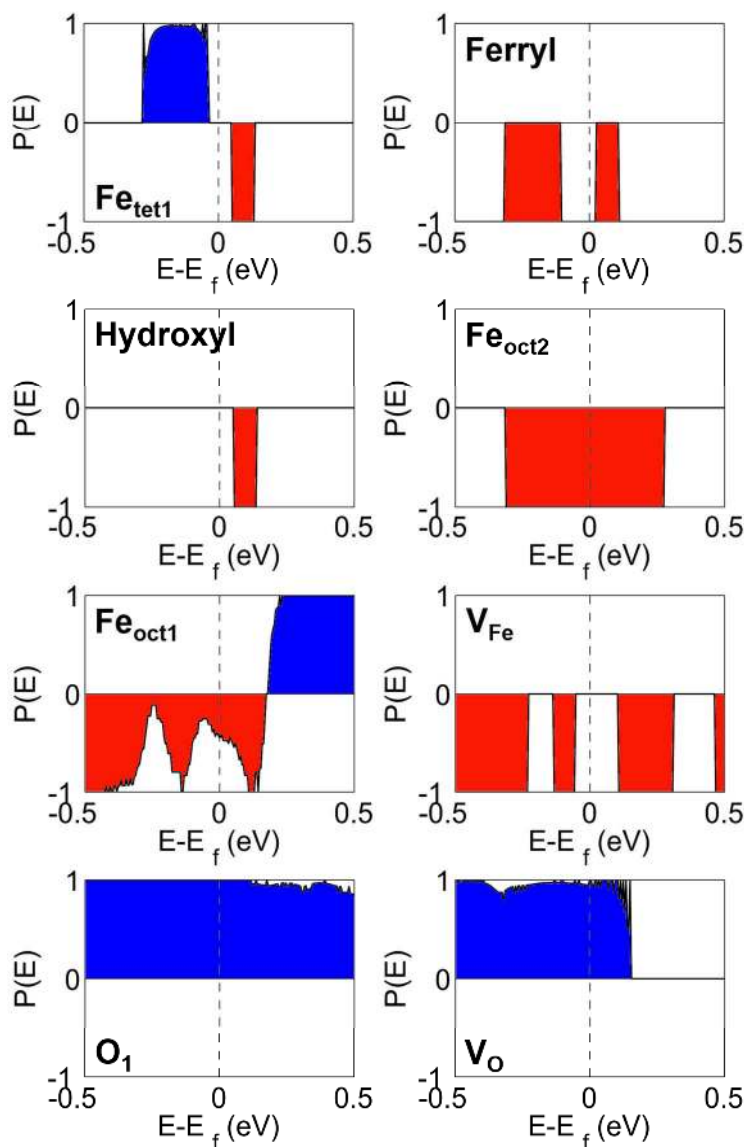
11   0.5 eV to +0.5 eV and -0.5 eV to +0.15 eV, respectively.

Figure 9. Spin polarization as a function of energy, P(E), calculated for eight terminations within [E_f-0.5 eV, E_f+0.5 eV] The vertical dotted lines indicate the Fermi level. The blue regions correspond to positive spin polarization while the red ones indicate negative spin polarization.

IV. Conclusions

We have discussed the results of PBE+U calculations on modified terminations of

magnetite (111) in terms of their structural, electronic, and magnetic properties and

1   compared them to the bulk-terminated surfaces. The most probable surface

2   terminations for Fe_3O_4 were compared using their relative stabilities for the relevant

3   limiting regimes of oxygen chemical potentials. For the surfaces comprised of bulk-like

4   terminations, the Fe_{tet1}-terminated surface has the lowest surface energy over a wide

5   range of oxygen chemical potentials while Fe_{oct2} becomes more stabilized in the oxygen

6   poor limit. Importantly, the surfaces that contain either oxygen adatoms or cationic

7   vacancies are calculated to be close in stability to the Fe_{tet1} surface at oxygen-rich and

8   oxygen-poor conditions, respectively. These modified surfaces with adsorbates or

9   cationic vacancies have significantly different surface geometries and electronic/

10   magnetic structures with respect to the previously considered structures without any

11   defects. In particular, these defects have a major impact on the electron redistributions

12   over surface layers, which lead to different spin polarizations near the Fermi level and

13   distinctive surface chemistries. Current work is in progress in our laboratories to

14   evaluate the impact of these surface chemistries on the nature of interfaces with organic

15   layers.

16

17   **Supporting Information**

18   Electronic Supplementary Information (ESI) available: The methodological details for

19   the range-separated hybrid functionals are given in Section S1. Convergence of

20   electronic properties with respect to slab thickness is given in Section S2. Analyses of

21   the surface stabilities and work functions using various DFT methodologies and

22   exchange-correlation functionals are given in S3 and S6. Tabulated data for the ionic

23   relaxations is given in Section 4. Section S5 shows the PDOS for bulk magnetite and all

seven terminations examined. Section S7 describes the layer-resolved spin polarization variation within PBE and hybrid functionals.

References

1. Gu, B. H.; Schmitt, J.; Chen, Z. H.; Liang, L. Y.; Mccarthy, J. F., Adsorption and Desorption of Natural Organic-Matter on Iron-Oxide - Mechanisms and Models. *Environ. Sci. Technol.* **1994,** *28* (1), 38-46.

2. Arbab, A. S.; Bashaw, L. A.; Miller, B. R.; Jordan, E. K.; Lewis, B. K.; Kalish, H.; Frank, J. A., Characterization of Biophysical and Metabolic Properties of Cells Labeled with Superparamagnetic Iron Oxide Nanoparticles and Transfection Agent for Cellular MR Imaging. *Radiology* **2003,** *229* (3), 838-846.

3. Sljukic, B.; Banks, C. E.; Compton, R. G., Iron Oxide Particles Are the Active Sites for Hydrogen Peroxide Sensing at Multiwalled Carbon Nanotube Modified Electrodes. *Nano Lett.* **2006,** *6* (7), 1556-1558.

4. Urbanova, V.; Magro, M.; Gedanken, A.; Baratella, D.; Vianello, F.; Zboril, R., Nanocrystalline Iron Oxides, Composites, and Related Materials as a Platform for Electrochemical, Magnetic, and Chemical Biosensors. *Chem. Mater.* **2014,** *26* (23), 6653-6673.

5. Gawande, M. B.; Branco, P. S.; Varma, R. S., Nano-magnetite (Fe_3O_4) as a Support for Recyclable Catalysts in the Development of Sustainable Methodologies. *Chem. Soc. Rev.* **2013,** *42* (8), 3371-3393.

6.   Arisi, E.; Bergenti, I.; Cavallini, M.; Riminucci, A.; Ruani, G.; Dediu, V.; Ghidini, M.; Pernechele, C.; Solzi, M., Direct Deposition of Magnetite Thin Films on Organic Semiconductors. *Appl. Phys. Lett.* **2008,** *93* (11), 113305.

7.   Zhang, D. D.; Feng, J.; Liu, Y. F.; Zhong, Y. Q.; Bai, Y.; Jin, Y.; Xie, G. H.; Xue, Q.; Zhao, Y.; Liu, S. Y.; Sun, H. B., Enhanced Hole Injection in Organic Light-Emitting Devices by Using Fe_3O_4 as an Anodic Buffer Layer. *Appl. Phys. Lett.* **2009,** *94* (22), 223306.

8.   Zhang, D. D.; Feng, J.; Zhong, Y. Q.; Liu, Y. F.; Wang, H.; Jin, Y.; Bai, Y.; Chen, Q. D.; Sun, H. B., Efficient Top-Emitting Organic Light-Emitting Devices Using Fe_3O_4 Modified Ag Anode. *Org. Electron.* **2010,** *11* (12), 1891-1895.

9.   Parkinson, G. S.; Diebold, U.; Tang, J.; Malkinsk, D. L., Tailoring the Interface Properties of Magnetite for Spintronics. In *Advanced Magnetic Materials*; Malkinsk, D. L., Ed.; InTech: Rijeka, Croatia, **2012**.

10.   Yoh, K.; Ohno, H.; Katano, Y.; Sueoka, K.; Mukasa, K.; Ramsteiner, M. E., Spin Polarization in Photo- and Electroluminescence of InAs and Metal/InAs Hybrid Structures. *Semicond. Sci. Technol.* **2004,** *19* (4), S386-S389.

11.   Fiederling, R.; Keim, M.; Reuscher, G.; Ossau, W.; Schmidt, G.; Waag, A.; Molenkamp, L. W., Injection and Detection of a Spin-polarized Current in a Light-Emitting Diode. *Nature* **1999,** *402* (6763), 787-790.

12.   Brown, P. J.; Neumann, K. U.; Webster, P. J.; Ziebeck, K. R. A., The Magnetization Distributions in Some Heusler Alloys Proposed as Half-metallic Ferromagnets. *J. Phys.: Condens. Matter* **2000,** *12* (8), 1827-1835.

13.   Bibes, M.; Villegas, J. E.; Barthélémy, A., Ultrathin Oxide Films and Interfaces for Electronics and Spintronics. *Adv. Phys.* **2011,** *60* (1), 5-84.

14.   Opel, M., Spintronic Oxides Grown by Laser-MBE. *J. Phys. D: Appl. Phys.* **2012,** *45* (3), 033001.

15.   Lai, C. H.; Huang, P. H.; Wang, Y. J.; Huang, R. T., Room-Temperature Growth of Epitaxial Fe_3O_4 Films by Ion Beam Deposition. *J. Appl. Phys.* **2004,** *95* (11), 7222-7224.

16.   Zhang, X.; Ma, Q.; Suzuki, K.; Sugihara, A.; Qin, G.; Miyazaki, T.; Mizukami, S., Magnetoresistance Effect in Rubrene-Based Spin Valves at Room Temperature. *ACS Appl. Mater. Interfaces* **2015,** *7* (8), 4685-4692.

17.   Bandyopadhyay, S.; Cahay, M., Introduction to Spintronics. CRC Press: Boca Raton, FL, **2008**; Chapter 12, p 515.

18.   Tobin, J. G.; Morton, S. A.; Yu, S. W.; Waddill, G. D.; Schuller, I. K.; Chambers, S. A., Spin Resolved Photoelectron Spectroscopy of Fe_3O_4: the Case Against Half-metallicity. *J. Phys.: Condens. Matter* **2007,** *19* (31), 315218.

19.   Pratt, A.; Kurahashi, M.; Sun, X.; Yamauchi, Y., Adsorbate-Induced Spin-Polarization Enhancement of Fe_3O_4(001). *J. Phys. D: Appl. Phys.* **2011,** *44* (6), 064010.

20.   Kurahashi, M.; Sun, X.; Yamauchi, Y., Recovery of the Half-metallicity of an Fe_3O_4(100) Surface by Atomic Hydrogen Adsorption. *Phys. Rev. B* **2010,** *81* (19), 193402.

21.   Freund, H. J., Adsorption of Gases on Complex: Solid Surfaces. *Angew. Chem. - Int. Ed.* **1997,** *36* (5), 452-475.

22.   Noguera, C., Polar Oxide Surfaces. *J. Phys.: Condens. Matter* **2000,** *12* (31), R367-R410.

23. Weiss, W.; Ranke, W., Surface Chemistry and Catalysis on Well-Defined Epitaxial Iron-oxide Layers. *Prog. Surf. Sci.* **2002,** *70* (1-3), 1-151.

24. Tannhauser, D. S., Conductivity in Iron Oxides. *J. Phys. Chem. Solids* **1962,** *23* (1–2), 25-34.

25. Verwey, E. J. W., Electronic Conduction of Magnetite (Fe_3O_4) and its Transition Point at Low Temperatures. *Nature* **1939,** *144*, 327-328.

26. Tsuda, N.; Nasu, K.; Fujimori, A.; Siratori, K., *Electronic Conduction in Oxides*. Springer-Verlag: Berlin; New York, **2000**.

27. Mizoguchi, M., NMR-Study of Low-Temperature Phase of Fe_3O_4. II. Electron Ordering Analysis. *J. Phys. Soc. Jpn.* **1978,** *44* (5), 1512-1520.

28. Wright, J. P.; Attfield, J. P.; Radaelli, P. G., Charge Ordered Structure of Magnetite Fe_3O_4 below the Verwey Transition. *Phys. Rev. B* **2002,** *66* (21), 214422.

29. Miyamoto, Y.; Shindo, M., Magnetoelectric Measurement of Magnetite (Fe_3O_4) at Low-Temperatures and Direct Evidence for Nonexistence of ac Mirror Plane. *J. Phys. Soc. Jpn.* **1993,** *62* (5), 1423-1426.

30. McCarty, K. F.; Monti, M.; Nie, S.; Siegel, D. A.; Starodub, E.; El Gabaly, F.; McDaniel, A. H.; Shavorskiy, A.; Tyliszczak, T.; Bluhm, H.; Bartelt, N. C.; de la Figuera, J., Oxidation of Magnetite(100) to Hematite Observed by In Situ Spectroscopy and Microscopy. *J. Phys. Chem. C* **2014,** *118* (34), 19768–19777.

31. Yu, X. H.; Li, Y. N.; Li, Y. W.; Wang, J. G.; Jiao, H. J., DFT+U Study of Molecular and Dissociative Water Adsorptions on the Fe_3O_4(110) Surface. *J. Phys. Chem. C* **2013,** *117* (15), 7648-7655.

32. Brown, G. E.; Henrich, V. E.; Casey, W. H.; Clark, D. L.; Eggleston, C.; Felmy, A.; Goodman, D. W.; Gratzel, M.; Maciel, G.; McCarthy, M. I.; Nealson, K. H.; Sverjensky, D. A.; Toney, M. F.; Zachara, J. M., Metal Oxide Surfaces and their Interactions With Aqueous Solutions and Microbial Organisms. *Chem. Rev.* **1999,** *99* (1), 77-174.

33. Zhao, L.; Zhang, H.; Xing, Y.; Song, S.; Yu, S.; Shi, W.; Guo, X.; Yang, J.; Lei, Y.; Cao, F., Morphology-Controlled Synthesis of Magnetites with Nanoporous Structures and Excellent Magnetic Properties. *Chem. Mater.* **2008,** *20* (1), 198-204.

34. Sato, J.; Kobayashi, M.; Kato, H.; Miyazaki, T.; Kakihana, M., Hydrothermal Synthesis of Magnetite Particles with Uncommon Crystal Facets. *J. Asian Ceram. Soc.* **2014,** *2* (3), 258-262.

35. Lodziana, Z., Surface Verwey Transition in Magnetite. *Phys. Rev. Lett.* **2007,** *99* (20), 206402.

36. Kendelewicz, T.; Kaya, S.; Newberg, J. T.; Bluhm, H.; Mulakaluri, N.; Moritz, W.; Scheffler, M.; Nilsson, A.; Pentcheva, R.; Brown, G. E., X-ray Photoemission and Density Functional Theory Study of the Interaction of Water Vapor with the Fe_3O_4(001) Surface at Near-Ambient Conditions. *J. Phys. Chem. C* **2013,** *117* (6), 2719-2733.

37. Bliem, R.; McDermott, E.; Ferstl, P.; Setvin, M.; Gamba, O.; Pavelec, J.; Schneider, M. A.; Schmid, M.; Diebold, U.; Blaha, P.; Hammer, L.; Parkinson, G. S., Subsurface Cation Vacancy Stabilization of the Magnetite(001) Surface. *Science* **2014,** *346* (6214), 1215-1218.

38. Zhou, Y.; Jin, X. S.; Mukovskii, Y. M.; Shvets, I. V., Kinetics of Oxidation of Low-Index Surfaces of Magnetite. *J. Phys.: Condens. Matter* **2004,** *16* (1), 1-12.

39. Yu, X. H.; Huo, C. F.; Li, Y. W.; Wang, J. G.; Jiao, H. J., Fe_3O_4 Surface Electronic Structures and Stability from GGA+U. *Surf. Sci.* **2012,** *606* (9-10), 872-879.

38

40.   Tasker, P. W., Stability of Ionic-Crystal Surfaces. *J. Phys. C* **1979,** *12* (22), 4977-4984.

41.   Lennie, A. R.; Condon, N. G.; Leibsle, F. M.; Murray, P. W.; Thornton, G.; Vaughan, D. J., Structures of Fe_3O_4(111) Surfaces Observed by Scanning Tunneling Microscopy. *Phys. Rev. B* **1996,** *53* (15), 10244-10253.

42.   Cutting, R. S.; Muryn, C. A.; Thornton, G.; Vaughan, D. J., Molecular Scale Investigations of the Reactivity of Magnetite with Formic Acid, Pyridine, and Carbon Tetrachloride. *Geochim. Cosmochim. Acta* **2006,** *70* (14), 3593-3612.

43.   Zhu, L.; Yao, K. L.; Liu, Z. L., First-principles Study of the Polar (111) Surface of Fe_3O_4. *Phys. Rev. B* **2006,** *74* (3), 035409.

44.   Ahdjoudj, J.; Martinsky, C.; Minot, C.; Van Hove, M. A.; Somorjai, G. A., Theoretical Study of the Termination of the Fe_3O_4(111) Surface. *Surf. Sci.* **1999,** *443* (1-2), 133-153.

45.   Ritter, M.; Weiss, W., Fe_3O_4(111) Surface Structure Determined by LEED Crystallography. *Surf. Sci.* **1999,** *432* (1-2), 81-94.

46.   Shaikhutdinov, S. K.; Ritter, M.; Wang, X. G.; Over, H.; Weiss, W., Defect Structures on Epitaxial Fe_3O_4(111) Films. *Phys. Rev. B* **1999,** *60* (15), 11062-11069.

47.   Paul, M.; Sing, M.; Claessen, R.; Schrupp, D.; Brabers, V. A. M., Thermodynamic Stability and Atomic and Electronic Structure of Reduced Fe_3O_4(111) Single-crystal Surfaces. *Phys. Rev. B* **2007,** *76* (7), 075412.

48.   Shimizu, T. K.; Jung, J.; Kato, H. S.; Kim, Y.; Kawai, M., Termination and Verwey Transition of the (111) Surface of Magnetite Studied by Scanning Tunneling Microscopy and First-principles Calculations. *Phys. Rev. B* **2010,** *81* (23), 235429.

49.   Grillo, M. E.; Finnis, M. W.; Ranke, W., Surface Structure and Water Adsorption on Fe_3O_4(111): Spin-density Functional Theory and On-Site Coulomb Interactions. *Phys. Rev. B* **2008,** *77* (7), 075407.

50.   Kiejna, A.; Ossowski, T.; Pabisiak, T., Surface Properties of the Clean and Au/Pd Covered Fe_3O_4(111): DFT and DFT+U Study. *Phys. Rev. B* **2012,** *85* (12), 125414.

51.   Berdunov, N.; Murphy, S.; Mariotto, G.; Shvets, I. V., Atomically Resolved Spin-Dependent Tunneling on the Oxygen-Terminated Fe_3O_4(111). *Phys. Rev. Lett.* **2004,** *93* (5), 057201.

52.   Sala, A.; Marchetto, H.; Qin, Z. H.; Shaikhutdinov, S.; Schmidt, T.; Freund, H. J., Defects and Inhomogeneities in Fe_3O_4(111) Thin Film Growth on Pt(111). *Phys. Rev. B* **2012,** *86* (15), 155430.

53.   Nie, S.; Starodub, E.; Monti, M.; Siegel, D. A.; Vergara, L.; El Gabaly, F.; Bartelt, N. C.; de la Figuera, J.; McCarty, K. F., Insight into Magnetite's Redox Catalysis from Observing Surface Morphology during Oxidation. *J. Am. Chem. Soc.* **2013,** *135* (27), 10091-10098.

54.   Campbell, C. T.; Peden, C. H. F., Chemistry - Oxygen Vacancies and Catalysis on Ceria Surfaces. *Science* **2005,** *309* (5735), 713-714.

55.   Rim, K. T.; Eom, D.; Chan, S. W.; Flytzani-Stephanopoulos, M.; Flynn, G. W.; Wen, X. D.; Batista, E. R., Scanning Tunneling Microscopy and Theoretical Study of Water Adsorption on Fe_3O_4: Implications for Catalysis. *J. Am. Chem. Soc.* **2012,** *134* (46), 18979-18985.

56.   Cutting, R. S.; Muryn, C. A.; Vaughan, D. J.; Thornton, G., Substrate-Termination and H_2O-Coverage Dependent Dissociation of H_2O on Fe_3O_4. *Surf. Sci.* **2008,** *602* (6), 1155-1165.

57.   Kresse, G.; Furthmuller, J., Efficiency of Ab-initio Total Energy Calculations for Metals and Semiconductors Using a Plane-Wave Basis Set. *Comput. Mater. Sci.* **1996,** *6* (1), 15-50.

58.   Kresse, G.; Furthmuller, J., Efficient Iterative Schemes for Ab initio Total-energy Calculations Using a Plane-wave Basis Set. *Phys. Rev. B* **1996,** *54* (16), 11169-11186.

59.   Blochl, P. E., Projector Augmented-Wave Method. *Phys. Rev. B* **1994,** *50* (24), 17953-17979.

60.   Noh, J.; Osman, O. I.; Aziz, S.; Winget, P.; Brédas, J. L., A Density Functional Theory Investigation of the Electronic Structure and Spin Moments of Magnetite. *Sci. Tech. Adv. Mater.* **2014,** *15*, 044202.

61.   Anisimov, V. I.; Zaanen, J.; Andersen, O. K., Band Theory and Mott Insulators - Hubbard-U Instead of Stoner-I. *Phys. Rev. B* **1991,** *44* (3), 943-954.

62.   Perdew, J. P.; Burke, K.; Ernzerhof, M., Generalized Gradient Aapproximation Made Simple. *Phys. Rev. Lett.* **1996,** *77* (18), 3865-3868.

63.   Perdew, J. P.; Burke, K.; Ernzerhof, M., Generalized Gradient Approximation Made Simple (vol 77, pg 3865, 1996). *Phys. Rev. Lett.* **1997,** *78* (7), 1396-1396.

64.   Dudarev, S. L.; Botton, G. A.; Savrasov, S. Y.; Humphreys, C. J.; Sutton, A. P., Electron-Energy-Loss Spectra and the Structural Stability of Nickel Oxide: An LSDA+U Study. *Phys. Rev. B* **1998,** *57* (3), 1505-1509.

65.   Monkhorst, H. J.; Pack, J. D., Special Points for Brillouin-Zone Integrations. *Phys. Rev. B* **1976,** *13* (12), 5188-5192.

66.   Blochl, P. E.; Jepsen, O.; Andersen, O. K., Improved Tetrahedron Method for Brillouin-Zone Integrations. *Phys. Rev. B* **1994,** *49* (23), 16223-16233.

67.   Bader, R. F. W.; Carroll, M. T.; Cheeseman, J. R.; Chang, C., Properties of Atoms in Molecules - Atomic Volumes. *J. Am. Chem. Soc.* **1987,** *109* (26), 7968-7979.

68.   Tang, W.; Sanville, E.; Henkelman, G., A Grid-based Bader Analysis Algorithm Without Lattice Bias. *J. Phys.: Condens. Matter* **2009,** *21* (8).

69.   Heyd, J.; Scuseria, G. E.; Ernzerhof, M., Hybrid Functionals Based on a Screened Coulomb Potential. *J. Chem. Phys.* **2003,** *118* (18), 8207-8215.

70.   Heyd, J.; Scuseria, G. E., Efficient Hybrid Density Functional Calculations in Solids: Assessment of the Heyd-Scuseria-Ernzerhof Screened Coulomb Hybrid Functional. *J. Chem. Phys.* **2004,** *121* (3), 1187-1192.

71.   Cornell, R. M.; Schwertmann, U., *The Iron Oxides : Structure, Properties, Reactions, Occurrences, and Uses*. 2nd ed.; Wiley-VCH: Weinheim, **2003**.

72.   Aragon, R., Magnetization and Exchange in Nonstoichiometric Magnetite. *Phys. Rev. B* **1992,** *46* (9), 5328-5333.

73.   Stull, D. R.; Prophet, H., JANAF Thermochemical Tables. In *NSRDS-NBS 37* [Online] 2d ed.; U.S. Dept. of Commerce, National Bureau of Standards: Washington, D.C., **1971**. http://purl.access.gpo.gov/GPO/LPS112842.

74.   Santos-Carballal, D.; Roldan, A.; Grau-Crespo, R.; de Leeuw, N. H., A DFT Study of the Structures, Stabilities and Redox Behaviour of the Major Surfaces of Magnetite Fe_3O_4. *Phys. Chem. Chem. Phys.* **2014,** *16* (39), 21082-21097.

75.   Govind, N.; Wang, Y. A.; da Silva, A. J. R.; Carter, E. A., Accurate Ab initio Energetics of Extended Systems via Explicit Correlation Embedded in a Density Functional Environment. *Chem. Phys. Lett.* **1998,** *295* (1-2), 129-134.

76.   Pople, J. A.; Headgordon, M.; Fox, D. J.; Raghavachari, K.; Curtiss, L. A., Gaussian-1 Theory - a General Procedure for Prediction of Molecular-Energies. *J. Chem. Phys.* **1989,** *90* (10), 5622-5629.

77.   Wang, L.; Maxisch, T.; Ceder, G., Oxidation Energies of Transition Metal Oxides within the GGA+U Framework. *Phys. Rev. B* **2006,** *73* (19), 195107.

78.   Franchini, C.; Podloucky, R.; Paier, J.; Marsman, M.; Kresse, G., Ground-State Properties of Multivalent Manganese Oxides: Density Functional and Hybrid Density Functional Calculations. *Phys. Rev. B* **2007,** *75* (19), 195128.

79.   Jain, A.; Hautier, G.; Ong, S. P.; Moore, C. J.; Fischer, C. C.; Persson, K. A.; Ceder, G., Formation Enthalpies by Mixing GGA and GGA+U Calculations. *Phys. Rev. B* **2011,** *84* (4), 045115.

80.   Hiura, S.; Ikeuchi, A.; Shirini, S.; Subagyo, A.; Sueoka, K., Effect of Adsorbed H Atoms on the Fe Electronic States of Fe_3O_4(001) Film Surfaces. *Phys. Rev. B* **2015,** *91* (20), 205411.

81.   Kendelewicz, T.; Liu, P.; Doyle, C. S.; Brown Jr, G. E.; Nelson, E. J.; Chambers, S. A., Reaction of Water with the (100) and (111) Surfaces of Fe_3O_4. *Surf. Sci.* **2000,** *453* (1–3), 32-46.

82.   Kiejna, A.; Pabisiak, T., Mixed Termination of Hematite (α-Fe_2O_3)(0001) Surface. *J. Phys. Chem. C* **2013,** *117* (46), 24339-24344.

83.   Shvets, I. V.; Mariotto, G.; Jordan, K.; Berdunov, N.; Kantor, R.; Murphy, S., Long-Range Charge Order on the Fe_3O_4(001) Surface. *Phys. Rev. B* **2004,** *70* (15), 155406.

84.   Rakhecha, V. C.; Murthy, N. S. S., Spin-Transfer Due to Covalency for Tetrahedral-Site Fe^{3+} Ions in Fe_3O_4. *J. Phys. C* **1978,** *11* (21), 4389-4404.

85.   Tatay, S.; Barraud, C.; Galbiati, M.; Seneor, P.; Mattana, R.; Bouzehouane, K.; Deranlot, C.; Jacquet, E.; Forment-Aliaga, A.; Jegou, P.; Fert, A.; Petroff, F., Self-Assembled Monolayer-Functionalized Half-Metallic Manganite for Molecular Spintronics. *ACS Nano* **2012,** *6* (10), 8753-8757.

86.   Dedkov, Y. S.; Rudiger, U.; Guntherodt, G., Evidence for the Half-metallic Ferromagnetic State of Fe_3O_4 by Spin-Resolved Photoelectron Spectroscopy. *Phys. Rev. B* **2002,** *65* (6), 064417.

87.   Pratt, A.; Kurahashi, M.; Sun, X.; Gilks, D.; Yamauchi, Y., Direct Observation of a Positive Spin Polarization at the (111) Surface of Magnetite. *Phys. Rev. B* **2012,** *85* (18), 180409(R).